A machine-learning architecture with two strategies for low-speed impact localization of composite laminates

Junhe Shen[a] , *Junjie Yea,*[b*] , *Zhiqiang Qu*[a] , *Lu Liu*[a] , *Wenhu Yang*[a] , *Yong Zhang*[a,c] , *Yixin Chen*[d]

Dianzi Liu [e*]

[a] Research Center for Applied Mechanics, Xidian University, Xi'an 710071, China

[b] Shaanxi Key Laboratory of Space Extreme Detection, Xidian University, Xi'an 710071, China

[c] Guodian Nanjing Automation Co., LTD.,Nanjing 211100, China

[d] Key Laboratory of Expressway Construction Machinery of Shaanxi Province, Chang'an University

[e] Engineering Division, Faculty of Science, University of East Anglia, Norwich, UK

*Corresponding authors.

Email address: ronkey6000@sina.com (Junjie Ye); Dianzi.Liu@uea.ac.uk (Dianzi Liu)

Abstract

In this paper, a machine-learning architecture with the integration of two strategies including data enhancement and adaptive generation scheme for Impact Localization (IL) are developed to address the aforementioned issues for location identification of impacts on composite laminates. Two main contributions are included in this research: First, response signals collected from low-speed impact experiments under various working conditions are denoised using Adaptive Sparse Noise Reduction Algorithm (ASNRA), which aims at maximizing the preservation of the original signal amplitude, thereby avoiding the underestimation of pulse features during denoising. Then a RIME-optimized Dual-layer Support Vector Regression (RDSVR) method for the real-time update of hyperparameters is implemented in the machine-learning architecture to realize IL. The superior performances of the IL architecture over different IL models are validated throughout the numerical examples in terms of stability and efficiency. Results demonstrate that proposed architecture has the ability to realize the accurate and robust IL of composite laminates.

Keywords: Composite materials; Impact localization; Machine learning; Sparse noise reduction; Optimization strategies

1. Introduction

Composite materials are widely used in industrial fields, including automotive[1, 2], aerospace[3, 4], oilfields[5], military[6, 7], and others, owing to their exceptional properties of being lightweight, corrosion-resistant, and high stiffness-to-weight ratio[8]. However, during operational service, they can be vulnerable to low-energy impact. Despite of impact as low as a few joules, they can result in severe delamination of composite laminates, leading to a significant reduction in structural strength. Therefore, identifying low-speed impact location has become an essential aspect of practical engineering applications. With the rise of artificial intelligence, it has found widespread applications of Impact Localization (IL) in composite materials. Recently, many scholars have applied various machine-learning methods to IL in composite materials and obtained promising results[9, 10]. However, significant noise interference is often present during the signal acquisition process, resulting in poor-quality response signal datasets and making accurate localization challenging.

Therefore, the removal of noise from response signals is a crucial strategy in the field of IL of composite material for fault diagnosis due to the presence of transient signals and noise components. In recent years, algorithms such as Empirical Mode Decomposition (EMD)[11], Ensemble Empirical Mode Decomposition(EEMD)[12], Spectral Kurtosis(SK)[13], and Wavelet Transform(WT)[14, 15] have been proven effective in enhancing the feature extraction capability of signals. Chen et al. [16] proposed a method for extracting weak fault features in rolling bearings using Improved Ensemble Noise-assisted Empirical Mode Decomposition (IENEMD) and Adaptive Threshold Denoising (ATD). Based on Improved Adaptive Resonance Technology (IART) to remove noise components from vibration signals, Li et al.[17] designed an improved EEMD. Shahis Hashim et al.[18] developed a novel denoising approach for fault diagnosis through the study of Spectral Kurtosis, employing a blind convolution strategy. However, the application of these algorithms to IL in composite materials presents certain challenges: (1) The noise reduction performance of traditional filtering algorithms depends highly on the characteristics of the measured signal. When the measured signal is complex or the noise is too strong, the denoising performance will be compromised. (2) During the process of eliminating noise or interference, the amplitude of the useful features is also reduced, potentially degrading the quality of the response signal dataset after denoising. In practical engineering applications, the collection of response signals often occurs in noisy environments, making it difficult for the aforementioned algorithms to extract signal features, resulting in poor denoising effects.

Since IL in composite laminates can be considered a regression problem[19], Lu et al.[20] achieved composite material damage location prediction based on Support Vector Regression (SVR) by extracting the wavelet packet energy spectrum of the Low-Velocity Impact (LVI) response signal monitored by FBG sensors. Datta et al.[21] used a SVR model based on the least squares method to assess the energy of x and y coordinate values on Carbon Fiber Reinforced Plastic (CFRP) plate-like structures. Compared to other nonlinear processes, SVR demonstrates strong generalization performance. However, these researchers used traditional techniques to determine the hyperparameters in SVR. The essence of this process is to combine different parameters to achieve the optimal results for SVR. Consequently, using traditional techniques for hyperparameter determination can lead to insufficient accuracy in predicting impact location and excessive time costs. The metaheuristic algorithms provide a solution to the problem. These algorithms replicate intelligent optimization functions inspired by various natural organisms [22]. There are multiple examples, such as the Artificial Bee Colony (ABC)[23], Bat Algorithm (BA)[24], Whale Optimization Algorithm (WOA)[25], Grasshopper Optimization Algorithm (GOA)[26], and Slime Mould Algorithm (SMA)[27]. The selection of the proper initial parameters and the utilization of the fitness function as the optimization core are critical for enhancing the overall optimization performance of the model. However, the traditional metaheuristic algorithms have problems such as falling into local optimum, large computational overhead, and high uncertainty in the large and small searching space.

In this paper, a machine-learning architecture with the integration of two methods is proposed to solve the challenges present in response signals. The first strategy (data enhancement) steps are as follows: (1) Adaptive Sparse Noise Algorithm (ASNRA) aims to extract useful signals in complex noise environments while preventing signal submersion by noise and maximizing the amplitude of the target signal component~~.~~ (2) a feature index with the fusion of dimensionality reduction method in the time domain, frequency domain, and time-frequency domain is developed to address issues such as insufficient accuracy caused by a single indicator in SVR. This approach facilitates comprehensive feature extraction, resulting in a new dataset with strong data interpretability. ~~Finally,~~

The second strategy (adaptive generation scheme) provides a Dual-layer Support Vector Regression (DSVR) method-whose hyperparameters are dynamically adjusted by the RIME algorithm, thereby significantly improving the accuracy of IL prediction and reducing time costs. The following sections of this paper are organized as follows: Section 2 presents the strategies and algorithms developed in the IL architecture. Section 3 analyzes the performance of the proposed architecture for low-speed IL of composite laminates throughout experimental tests. Finally, conclusions are provided in Section 4.

2. Constructing Architecture-Related Methodology

In this paper, the impact detection is performed by the SVR-based architecture, a data-driven positioning algorithm [32], for the position prediction. However, the SVR-based architecture has the issues including: (1) Noise interference with impact data affects the extraction accuracy from its characteristic amplitude. This will directly lead to poor prediction accuracy and a large deviation from the true results. (2) The architecture of SVR as the core requires the specific experience for parameter setting and tuning. Therefore, this causes the great increase of time costs and the lack of robustness of prediction results. To address these difficulties, this section provides two strategies, namely data enhancement and adaptive generation scheme for impact localization.

2.1 Data enhancement

The first method mainly plays its role in mitigating the influence of noise on the original data under complex and various working conditions, enabling the enhanced quality of datasets. The second method performs feature extraction on the dataset processed by the Adaptive Sparse Noise Reduction Algorithm(ASNRA), which is introduced by the section below and increases the dimension of the dataset. These two methods improve the capability of the stability and generalization.

2.1.1 Adaptive Sparse Noise Reduction Algorithm

ASNRA is a signal noise reduction algorithm that integrates Tunable-Q Wavelet Transform (TQWT) and Adaptive Generalized Minimax-Concave (AGMC). This combination maintains convexity and maximizes the sparsity of the objective function, properties that are beneficial for response signal noise reduction. The following is a description of these two algorithms.

(1) Tunable-Q Wavelet Transform

TQWT is a structured design methodology that dynamically adjusts parameters to comply with the property of wavelet basis functions. By combining the advances of continuous wavelet and second-generation wavelet transforms, TQWT overcomes the shortcomings of discrete wavelet transform. The oscillatory behavior of wavelet basis function is optimized through the adjustment of parameters, including the Q factor, r factor, and the number of decomposition levels J [33, 34]. This optimization guarantees optimal correspondence between the oscillatory features of wavelet basis functions and those of the measured signal. The schematic diagram of the TQWT filter structure is illustrated in Fig. 1, where the signal decomposition and reconstruction are accomplished by combining a dual-channel filter.

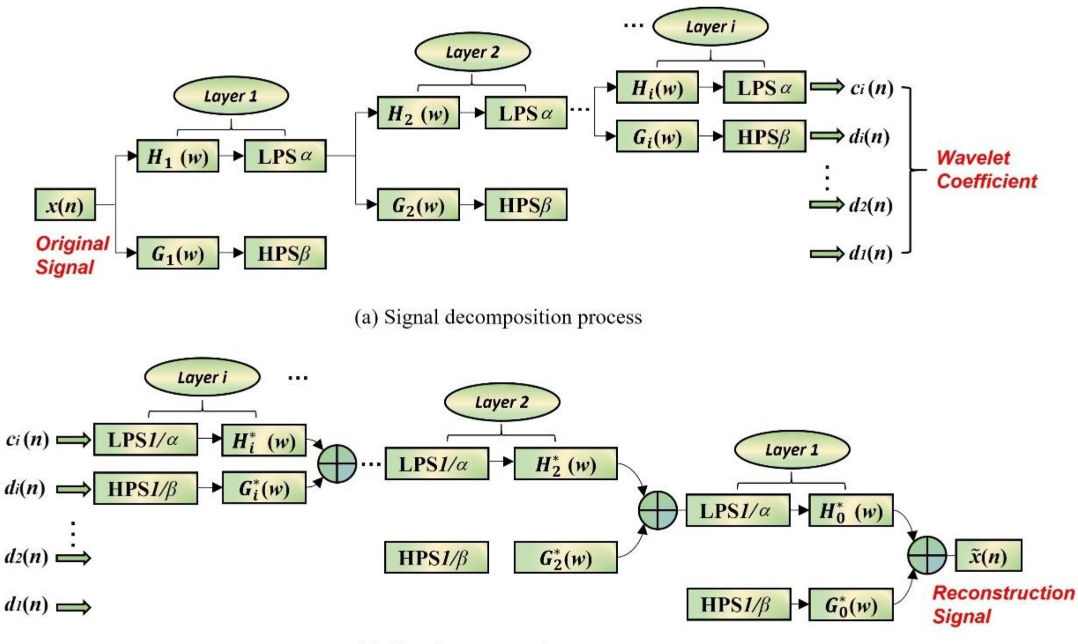

(a) Signal decomposition process

(b) Signal reconstruction process

Fig. 1. TQWT filter decomposition and reconstruction diagram

It should be noted that LPS and HPS denote the low-pass and high-pass scale expansions. $H_i(w)$ and $G_i(w)$ represent the low-frequency and the high-frequency response during decomposing or reconstructing at the i-th layer. α and β depict the corresponding scale transformation factors, which determine the transformation of the quality factor Q and redundancy coefficient r .

(2) Adaptive Generalized Minimax-Concave

A sparse-enhanced decomposition signal method based on the GMC penalty term is presented to reduce noise interference. In engineering applications, response signals generally contain the stress wave and noise at the points of the interest in the low-speed impact. Therefore, the response signal $y \in \mathbb{R}^{M}$ of the composite laminate can be formulated as follows[35]:

$$y = Ax + n \tag{1}$$

where $Ax \in \mathbb{R}^{M}$ and $n \in \mathbb{R}^{M}$ denote the clean signal and the noise component. The matrix operation is expressed through the operator $y \in \mathbb{R}^{M \times N}$ $(M < N)$.

According to the generalized Huber function and the definition of the GMC penalty function, substituting the GMC penalty function $\psi_B : \mathbb{R}^{N} \to \mathbb{R}$ into the objective function combined with GMC[36], one has:

$$\begin{aligned} F(x,v) &= \frac{1}{2} \| y - Ax \|_2^2 + \lambda \psi_B(x) \\ &= \max_{v} \{ \frac{1}{2} \| y - Ax \|_2^2 + \lambda \| \mathrm{x} \|_1 - \lambda \| v \|_1 - \frac{\lambda}{2} \| B(x - v) \|_2^2 \} \\ &= \frac{1}{2} x^T (A^T A - \lambda B^T B) x + \lambda \| x \|_1 + \max_{v \in \mathbb{R}^{N}} g(x,v) \end{aligned} \tag{2}$$

where $g(x,v)$ is an expression that is convex regarding x, to ensure the overall convexity of the function $F(x)$. It is necessary to satisfy the inequality $A^T A - \lambda B^T B \geq 0$, which can be further transformed when $0 \leq \gamma \leq 1$ and $B = \sqrt{\gamma / \lambda} A$ are achieved. The matrix A still allows the function $F(x)$ to maintain overall convexity. Fig. 2 depicts the non-convex curves of the generalized Huber function and the GMC penalty function. The minimization points can be identified, ensuring the final solution's uniqueness and the extracted features' sparsity.

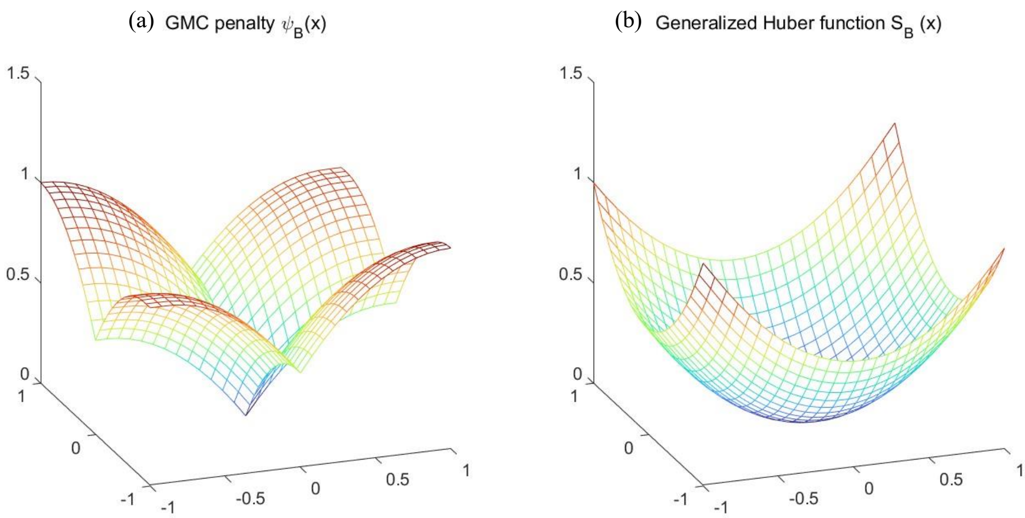

Fig. 2. (a) GMC penalty and (b) Generalized Huber function

Additionally, taking the Root Mean Square Error（RMSE）as a quantification metric, a dynamic regularization parameter λ is employed to analyze the simulated signals. Considering an adaptive parameter λ ranging from 0 to 2 (with an increment of 0.05), the adaptive setting minimizes RMSE, resulting in an optimal γ value of 0.63. The Proximal Gradient Method (PGM) ensures the global minimization of the non-convex sparse regularization function. The GMC penalty regularization problem is reformulated into a saddle-point problem as follows:

$$(x^{opt}, v^{opt}) = \arg\min_{x\in\mathbb{R}^N}\max_{v\in\mathbb{R}^N} F(x,v) \tag{3}$$

where optimizing the function $F(x,v)=\frac{1}{2}\|y-Ax\|_2^2+\lambda\|x\|_1-\lambda\|v\|_1-\frac{\lambda}{2}\|A(x-v)\|_2^2$ is a saddle-point problem, in which it can be solved by the Forward Backward Splitting (FBS) algorithm. The variable μ in the FBS should satisfy the condition $0\le\mu\le\frac{2}{\max\{1,\gamma/(1\text{-}\gamma)\}\left\|A^T A\right\|_2}$.

2.1.2 Multidimensional Indicator Fusion

A new feature dataset is formed by extracting time domain, frequency domain, and time-frequency domain features from the vibration response signal. This dataset offers advantages such as low operating costs and strong interpretability, addressing impact of insufficient data dimensions in small sample scenarios. Various types of feature indicators extracted from the dataset after ASNRA noise reduction are developed as follows:

(1) Time Domain indicators

Time-domain features are mainly divided into two categories: the first category consists of dimensional statistical parameters, including the mean value TD_1, the standard deviation TD_2, the variance value TD_3, the maximum value TD_4, the minimum value TD_5, the peak-to-peak value TD_6, the root mean square TD_7, the absolute mean value TD_8, and the square root amplitude TD_9. The second category includes dimensionless statistical parameters including the skewness factor TD_{10}, the kurtosis factor TD_{11}, the waveform factor TD_{12}, the kurtosis factor TD_{13}, the pulse factor TD_{14}, and the margin factor TD_{15}. Table 1 describes the calculation methods for each statistical parameter.

Table 1. Time domain metrics calculation formulas (N is the number of sampling points in the low-speed impact response signal $s(t)$)

Formula	Formula	Formula	Formula
$TD_1 = \frac{1}{N}\sum_{t=1}^{N} s(t)$	$TD_5 = min(s(t))$	$TD_9 = (\frac{1}{N}\sum_{t=1}^{N}\sqrt{\lvert s(t)\rvert})^2$	$TD_{13} = \frac{TD_4}{TD_7}$
$TD_2 = \sqrt{\frac{1}{N}\sum_{t=1}^{N}(s(t) - TD_1)^2}$	$TD_6 = TD_4 - TD_5$	$TD_{10} = \frac{1}{N}\frac{\sum_{t=1}^{N} s^3(t)}{TD_7^3}$	$TD_{14} = \frac{TD_4}{TD_8}$
$TD_3 = \frac{1}{N}\sum_{t=1}^{N}(s(t) - TD_1)^2$	$TD_7 = \sqrt{\frac{1}{N}\sum_{t=1}^{N} s^3(t)}$	$TD_{11} = \frac{1}{N}\frac{\sum_{t=1}^{N} s^4(t)}{TD_7^4}$	$TD_{15} = \frac{TD_4}{TD_9}$
$TD_4 = max(s(t))$	$TD_8 = \left\lvert \frac{1}{N}\sum_{t=1}^{N} s(t) \right\rvert$	$TD_{12} = \frac{TD_7}{TD_8}$	

(2) Frequency Domain indicators

Frequency performance indicators include the average frequency FD_1, the centroid frequency FD_2, the root mean square frequency FD_3, the mean square frequency FD_4, the standard deviation frequency FD_5, and the kurtosis frequency FD_6. The calculation methods for these five frequency performance indicators are described in Table2, where $\varphi(f)$ represents the spectrum of response signal $s(t)$. The parameter K is the number of Fourier transform points for $s(t)$ and F_f represents the frequency corresponding to each Fourier transform point.

Table 2. Frequency domain metrics calculation formulas

Formula	Formula	Formula
$FD_1 = \frac{1}{K}\sum_{f=1}^{K}\varphi(f)$	$FD_2 = \frac{\sum_{f=1}^{K} F_f \varphi(f)}{\sum_{f=1}^{K}\varphi(f)}$	$FD_3 = \sqrt{\frac{\sum_{f=1}^{K} F_f^2 \varphi(f)}{\sum_{f=1}^{K}\varphi(f)}}$
$FD_4 = \frac{\sum_{f=1}^{K} F_f^2 \varphi(f)}{\sum_{f=1}^{K}\varphi(f)}$	$FD_5 = \sqrt{\frac{\sum_{f=1}^{K}(F_f - FD_2)^2 \varphi(f)}{K}}$	$FD_6 = \frac{\sum_{f=1}^{K}(F_f - FD_2)^4 \varphi(f)}{K \times FD_5}$

(3) Time-Frequency Domain indicators

Applying the Short-time Fourier transform (STFT) [37] to analyze signals that change over time, the frequencies and phases of local signals are calculated at each moment by the determination of the maximum amplitude at each frequency. Subsequently, by calculating dimensionless and dimensioned statistical parameters from the generated data sequence, 15 time-frequency domain features parameters are obtained.

2.2 Adaptive generation scheme for Impact Localization

2.2.1 Dual-layer Support Vector Regression (DSVR) algorithm

The Adaptive generation scheme is developed on the basis of DSVR to predict the impact location. SVR is usually used to solve a continuous data regression problems[32]. Assume that the training dataset is $\{(x_i, y_i) | i = 1, 2 \ldots s\}$ and s represents the sample number. The SVR incorporates the Lagrange multiplier method, facilitating its transformation into a dual problem. By introducing a kernel function, the algorithm has the ability to calculate inner products within the same feature space, addressing issues of linear inseparability in datasets. This augmentation enhances the universality of the SVR, and its expression is formulated as follows:

$$\min_{\omega} \frac{1}{2}\|\omega\|^2 + c\sum_{i=1} s\xi_i + \xi_i^* \quad s.t. \begin{cases} y_i - \omega \cdot \phi(x_i) - b \le \varepsilon + \xi_i \\ \omega \cdot \phi(x_i) + b - y_i \le \varepsilon + \xi_i^* \\ \xi_i, \xi_i^* \ge 0 \end{cases} \tag{4}$$

where the parameters ω and c represent the weight factor and the penalty factor, respectively. ξ_i and ξ_i^* are the slack variables. $\phi(x)$ and ε are respectively the mapping function and the insensitive loss function. The symbol b indicates the function threshold.

In the scenario with a limited sample size, this study utilizes the Radial Basis Function（RBF） as a kernel function for the SVR. It divides the extracted multi-domain indicator features from low-speed response signals into training and testing datasets, which are then input into the SVR. Naturally, a mapping relationship between the multi-domain indicator features of the input signals and the impact coordinates enables the prediction of low-speed impact points on composite laminates. Two sets of SVR are configured to build the mapping relationships for the x-coordinate and y-coordinate values separately. Sequentially arranging the predicted coordinates, DSVR is assembled. Fig. 3 illustrates the structure and functionality of DSVR.

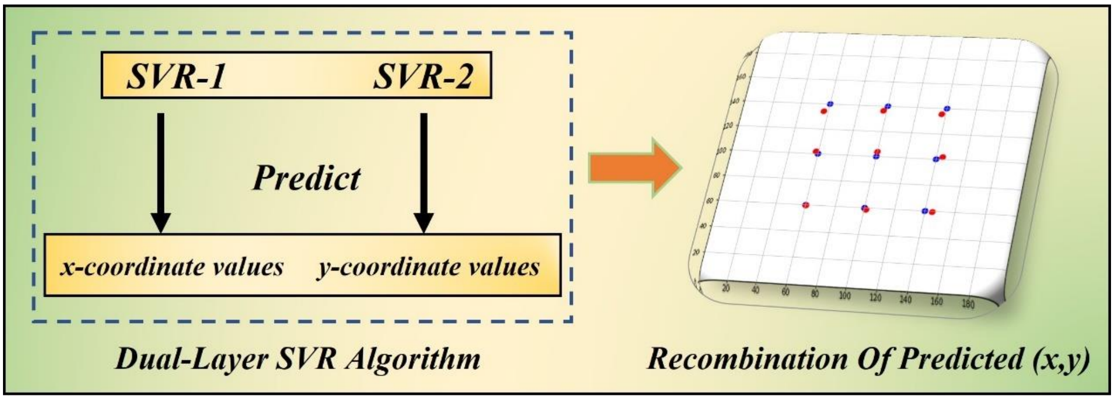

Fig. 3. Dual-Layer SVR display

2.2.2 Brief review of RIME

The complexity and recognition accuracy of the developed DSVR are closely dependent on the kernel parameter γ and penalty parameter C. In detail, a small kernel parameter γ combined with a large penalty function C may result in overfitting[38]. In order to achieve the adaptive optimization of the parameters mentioned above, the RIME proposed by Su[39] is a novel metaheuristic algorithm to investigate the soft-rime and hard-rime growth processes of ice in nature and is implemented in DSVR. This paper adopts the RIME algorithm, utilizing the RMSE as the fitness function to implement the search of the solution space. Based on the above conditions, a method (the RIME-optimized dual-layer Support Vector Regression, RDSVR) integrating RIME and DSVR is defined to predict coordinate values in the event of a low-speed impact. As the main part of RDSVR, RIME is described below.

RIME is a meta-heuristic algorithm consisting of Soft-rime searching strategy and the Hard-rime puncture mechanism. The rime-population R is used to represent the frost-ice growth process, which can be directly formulated by the hoar frost particle x_{ij} as follows,

$$R = \begin{bmatrix} x_{11} & x_{12} & \cdots & x_{1j} \\ x_{21} & x_{22} & \cdots & x_{2j} \\ \vdots & \vdots & \ddots & \vdots \\ x_{i1} & x_{i2} & \cdots & x_{ij} \end{bmatrix} \tag{5}$$

where the subscripts i and j represent the number of rime body rime particle, respectively. The particle position R_{ij}^{new} in the soft-rime search strategy is updated as follows:

$$R_{ij}^{new} = R_{best,j} + r_1 \cdot \cos\left(\pi \cdot \frac{t}{10 \cdot T}\right) \cdot \beta \cdot \left(h \cdot \left(Ub_{ij} - Lb_{ij}\right) + Lb_{ij}\right) \tag{6}$$

$$r_2 < E \tag{7}$$

where the subscripts i and j denote the i-th and j-th particle of the rime-agent. $R_{best,j}$ indicates the best rime-agent in the rime-population R. The parameter r_1 is a random number within the range from -1 to 1, which is closely related to the direction of particle movement. The symbols t and T represent the current iteration number and the maximum iteration number, respectively. h is an adhesion coefficient within the range from 0 to 1, controlling the distance between the centers of two rime particles. Ub_{ij} and Lb_{ij} are the upper and lower bounds in the escape space and constrain the effective region of particle motion. β is the environmental factor to ensure the convergence of the algorithm.

In the hard-rime puncture mechanism, the particle replacement formula is defined as follows:

$$R_{ij}^{new} = R_{best,j} \tag{8}$$

$$r_3 < F_{norm}\left(S_i\right) \tag{9}$$

where R_{ij}^{new} is the new position of the updated particle and $R_{best,j}$ is the j-th particle of the best rime-agent in the rime-population R. F_{norm} represents the normalized fitness value of the current agent and indicates the probability of selection the i-th rime-agent. r_3 is a random number within the range (-1,1).

Combining the soft-rime searching strategy with the hard-rime puncture mechanism, an improved positive greedy selection mechanism is developed for the better global exploration efficiency. The RIME-based DSVR possesses the following advantages:

(1) The ability to rapidly locate a globally approximate optimal solution.

(2) The improvement of a robust algorithm demonstrating the capability of global exploration.

(3) The ability to seamless transition between the large and small searching space.

Based on the two strategies proposed above, the IL architecture to predict impact location is developed and its flowchart is shown in Fig. 4. The specific steps are listed as follows:

(1) Data Collection: Utilizing acceleration sensors to collect the low-speed impact signals.

(2) Data Enhancement: ASNRA is employed to denoise the collected response signals and to obtain the reconstructed response signal. On this basis, multi-dimensional indicator features from the response signal are extracted before the fusion with a multidimensional indicator feature dataset.

(3) RDSVR Iteration: The enhanced dataset is divided into training and testing datasets for model constructing. Parameters are adaptively selected corresponding to the minimum fitness function during the process.

(4) RDSVR Prediction: The optimal parameters are applied to the regression training and the coordinate prediction, and the result image is displayed intuitively.

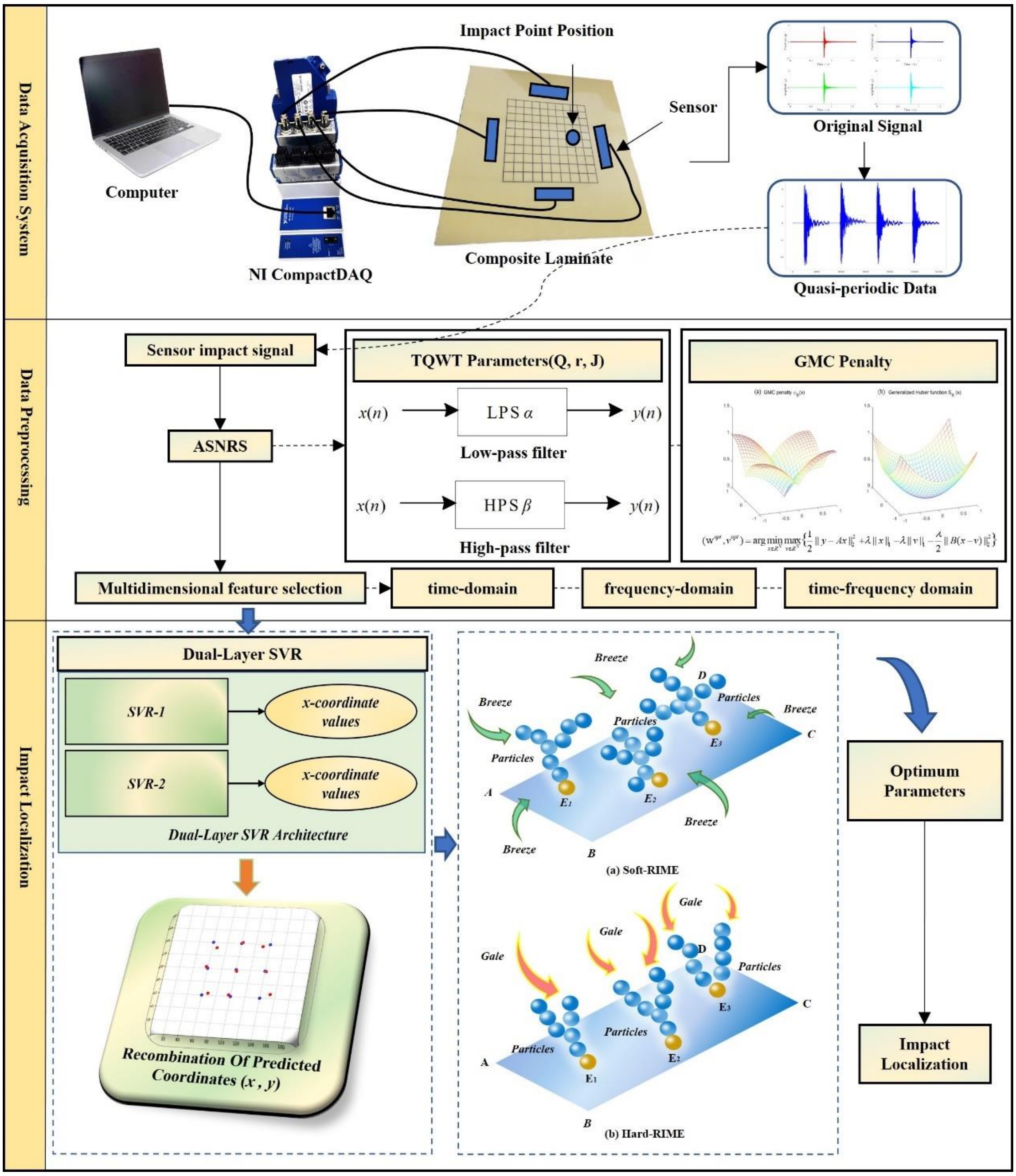

Fig. 4. Flow chart of impact localization architecture based on ASNRA

3.Experimental demonstration

3.1 Low-speed impact experiment

To conduct low-speed impact experiments for the investigation of IL, the glass fiber reinforced epoxy resin composite laminates ($400mm \times 400mm \times 6mm$) with resin content of 40%, density of $1.8 \times 10^3 kg/m^3$ and Poisson 's ratio of 0.3 are selected in this study. The laminates are evenly divided into 100 regions with the labels A1-A100 and the impact position are marked by an asterisk shown in Fig. 5. Considering that composite materials often serve in harsh environments, ceramic products with stainless steel shells are selected as sensing devices, whose configurations include a weight of 13 g and a dimension of $\phi 12 \times 17mm$. To efficiently conduct the prediction of the impact position, a monitoring area ($200mm \times 200mm \times 6mm$) located at the center of the laminate is defined to study IL.

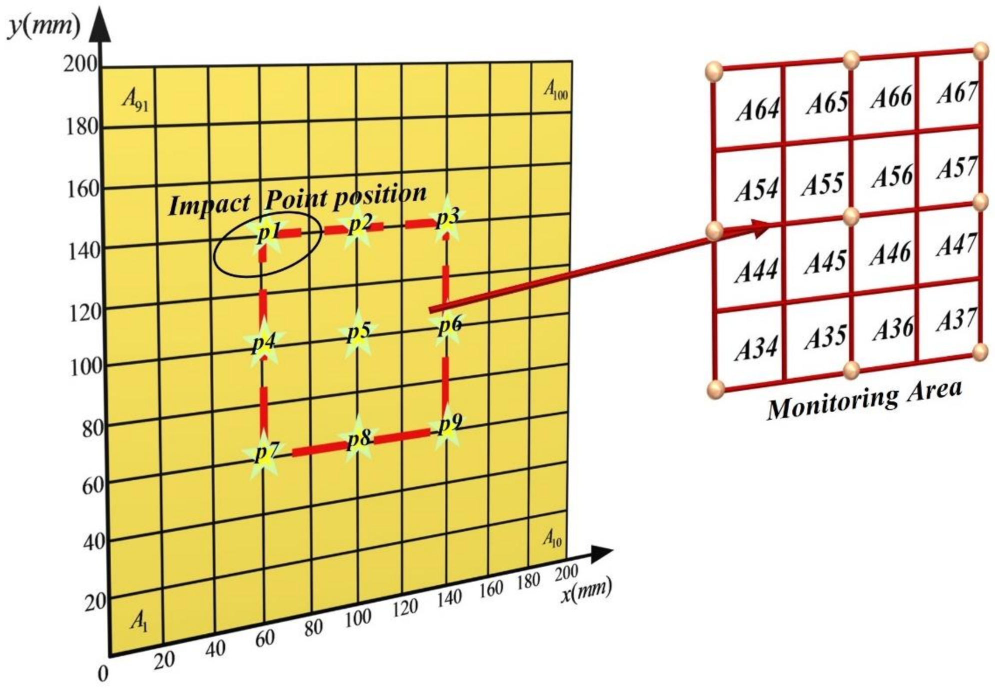

Fig. 5. Impact locations of the monitored composite laminate

To simulate the low-speed impact in engineering applications, a steel ball with a weight of 10g is used for free fall at a height of 15cm, and an impact energy of 0.0147J is estimated. A data acquisition system including I-TY100 accelerometer sensor, NI CompactDAQ (NI-CDAQ9184 Chassis, NI-9234 (Vibration Input Module)), and LabVIEW data acquisition software, is set up to monitor the response signal in Fig. 6. During the experiment, four accelerometer sensors are connected to the data acquisition system, and the LabVIEW software is employed to collect the vibration response data. Moreover, the experimental environment is set to mitigate the noise exposure for the clean signal acquisition. In the multi-channel acquisition, the signals among the channels affect each other, the higher the sampling rate, the greater the impact. This issue could be addressed by reducing the sampling frequency, thus in this research the sampling frequency is set to 15 kHz. The specific steps of the experiment are provided as follows: (1) The grid is used to discretize the monitoring area, and the distance between the grids is 20 mm. A total of 9 points are selected as the impact position, and the division position and number are shown in Fig. 5 (2) Each of the 9 impact points is sequentially impacted, and data are collected 25 times for each point to construct the dataset.

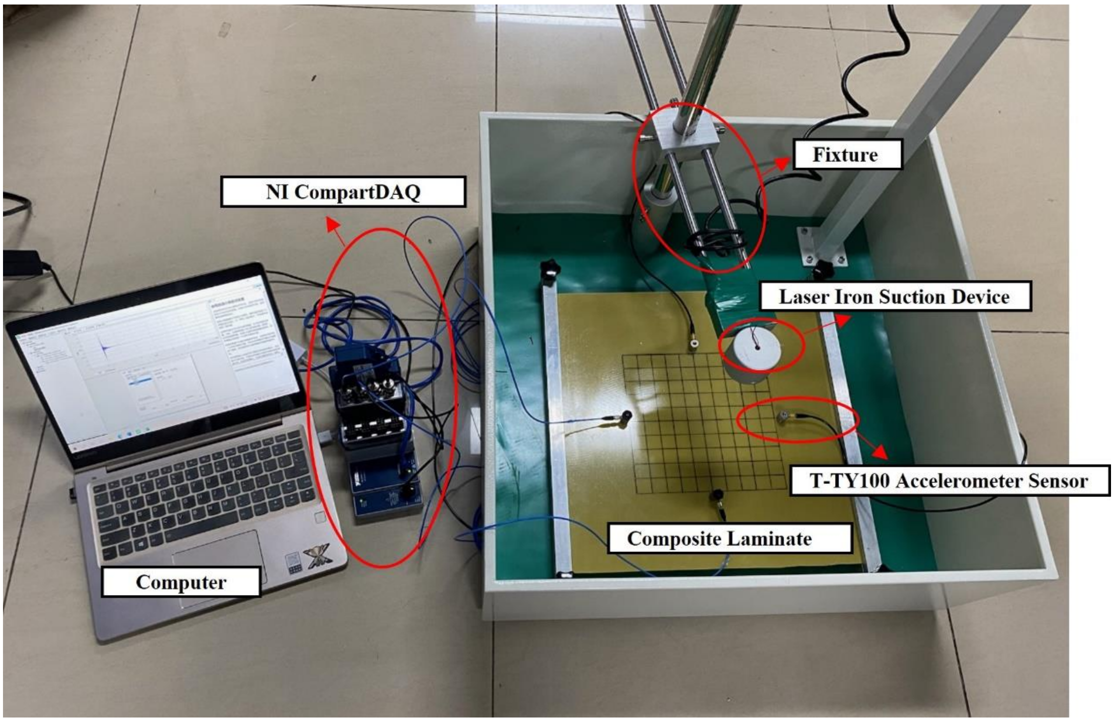

Fig. 6. Experimental Acquisition System

3.2 Data preprocessing

Data preprocessing is essential to improve the localization accuracy. It involves the periodic fitting adding different noises to the signal. These operations also can ensure effective data enhancement in the scenarios with a small number of samples.

3.2.1 Periodic Fitting

A set of datasets collected by different sensors at the same point under the same impact condition are obtained to identify the difference of characteristic amplitude. As observed in Fig. 7 (a), the time-domain responses represented by four sensors are almost same. Therefore, quasi-periodic data analysis is conducted in this research. Following that, ASNRA is applied to process the response signals considering different levels of noises. First, 3000 points in the vicinity of the maximum amplitude of the sampling data from each sensor are extracted and combined into a quasi-periodic signal. The integrated signal of the quasi-periodic response is presented in Fig. 7 (b). According to Fig. 7 (c), the fitted quasi-periodic signal has shown a degree of periodical performance with the period of 0.2s by the integration scheme and the frequency of the spectrum is 6.25 Hz. Also, it is noted that the double, the triple, and the quadruple frequencies are 11.25 Hz, 16.25 Hz and 21.25 Hz, respectively. The scheme can greatly retain the characteristics of the shock response data and facilitate the dimensionality reduction of the response signal in different noise environments. By this study, the rationality and effectiveness of the fitting scheme are demonstrated.

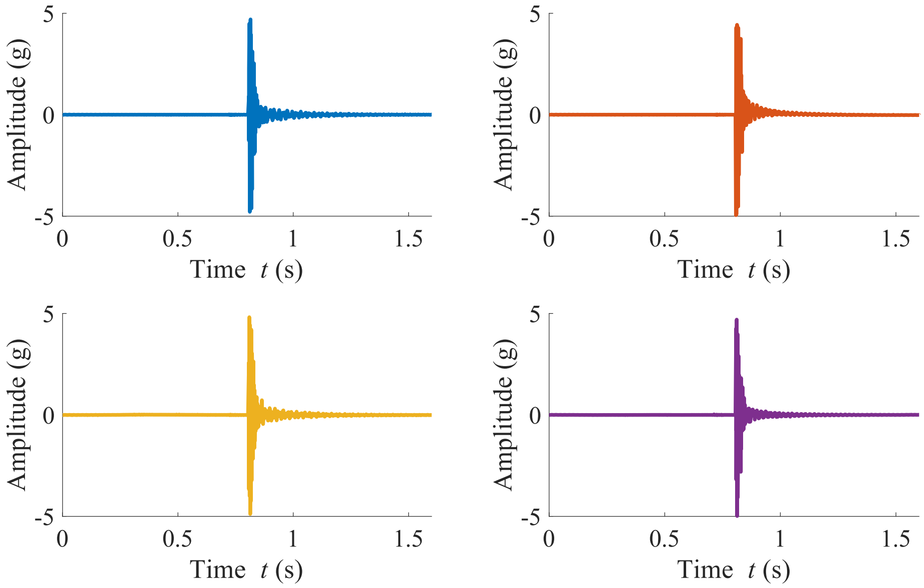

(a) Time domain diagram of original signal

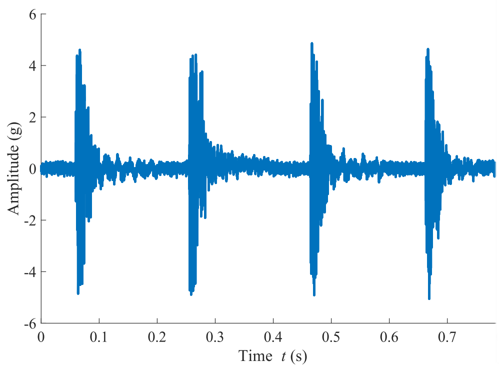

(b) Quasi-periodic response signals

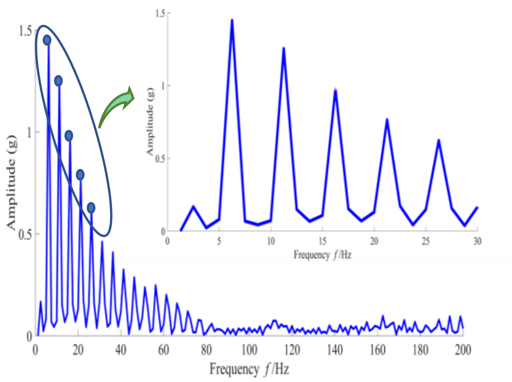

(c) Quasi-periodic response signal Hilbert envelope spectrum

Fig. 7. Comparison of original signal images (a) the integrated quasi-periodic signal (b) Quasi-periodic response signal (c) Hilbert envelope spectrum

3.2.2 Denoising capability of ASNRA

In order to verify the denoising capability of various algorithms in different noise environments, the noise with standard deviations of 0.1,0.3,0.5 and 0.7 is added to the dataset to represent real working conditions. Comparisons of the quasi-periodic response signals in the time domain considering the addition of various noise are conducted to study the robustness of the architecture proposed in this paper. Fig. 8 shows a total of 5 response signals recorded under complex working conditions. The green curve represents the original response signal without the consideration of noise. The purple, yellow, orange, and blue curves represent response signals in the time domain considering the addition of noise with standard deviations of 0.1, 0.3, 0.5 and 0.7, respectively. It can be observed that as the noise gradually increases, the response signal is significantly affected and its characteristics cannot be easily identified. Therefore, it is necessary to perform the denoising process for data enhancement of the response signal and the increase of Signal-to-Noise Ratio (SNR).

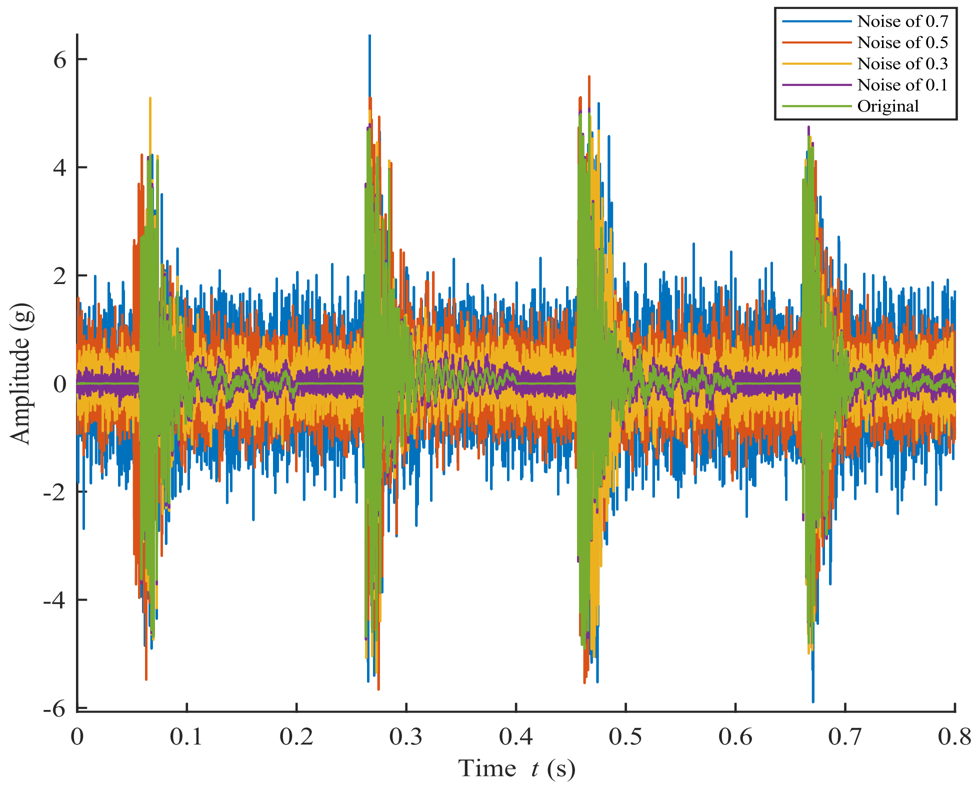

Fig. 8. Time domain diagram of response signal under complex working conditions and noise-free conditions

3.3 Performance Comparison

The performance of the IL architecture depends on both ASNRA and RDSVR. ASNRA guarantees the result accuracy, and RDSVR is a critical step to realize the localization prediction in the process of impact localization by the proposed architecture. Section 3.3.1 aims to the performance verification of ASNRA and includes the result comparison with other noise reduction algorithms. The parameter settings and evaluation index selection of RDSVR for IL are provided in Section 3.3.2. Finally, the experimental results by the proposed method are provided in Sections 3.3.3 and 3.3.4.

3.3.1 Comparison of noise reduction using different algorithms

In this study, three variable parameters ($Q = 3$, $r = 3$ and $J = 10$) in TQWT, the non-convex penalty function ($\gamma = 0.36$) in the GMC and the non-convexity parameter ($\lambda = 0.53$) are set to ensure the best performance of ASNRA. In Fig.9, the effect of different noise levels on the response signal is demonstrated by A1-1 - A1-4 using ASNRA. The red curves represent the denoised low-speed response signals, and the blue curves denote the low-speed response signals with the addition of noise with standard variation of 0.1, 0.3, 0.5 and 0.7. Moreover, the images labelled with B, C, and D in Fig. 9 are the time-domain responses under the consideration of denoising by EMD, EEMD, and VMD, respectively. It can be observed that the time-domain responses obtained by ASNRA clearly include the characteristics of the signal, and effectively retain the amplitude information during the denoising process. As the noise pollution becomes more and more serious, the clean response signal is gradually wrapped in the noise, resulting in the higher demand for denoising. As compared with other algorithms, it is demonstrated that the ASNRA has the ability to robustly solve the problem under various noise environments. According to Table 3, RMSE and Signal-to-Noise Ratio (SNR) are used to assess noise reduction performance. It is noted that when a good RMSE is considered, only the SNR of the response signal after noise reduction by ASNRA is positive and further improved by 125.3 %. For other algorithms, the SNR values are all negative. In general, ASNRA can preserve the signal amplitude well whilst realizing the denoising capability, leading to the clearer impact features extracted than the results by EMD, EEMD, and VMD.

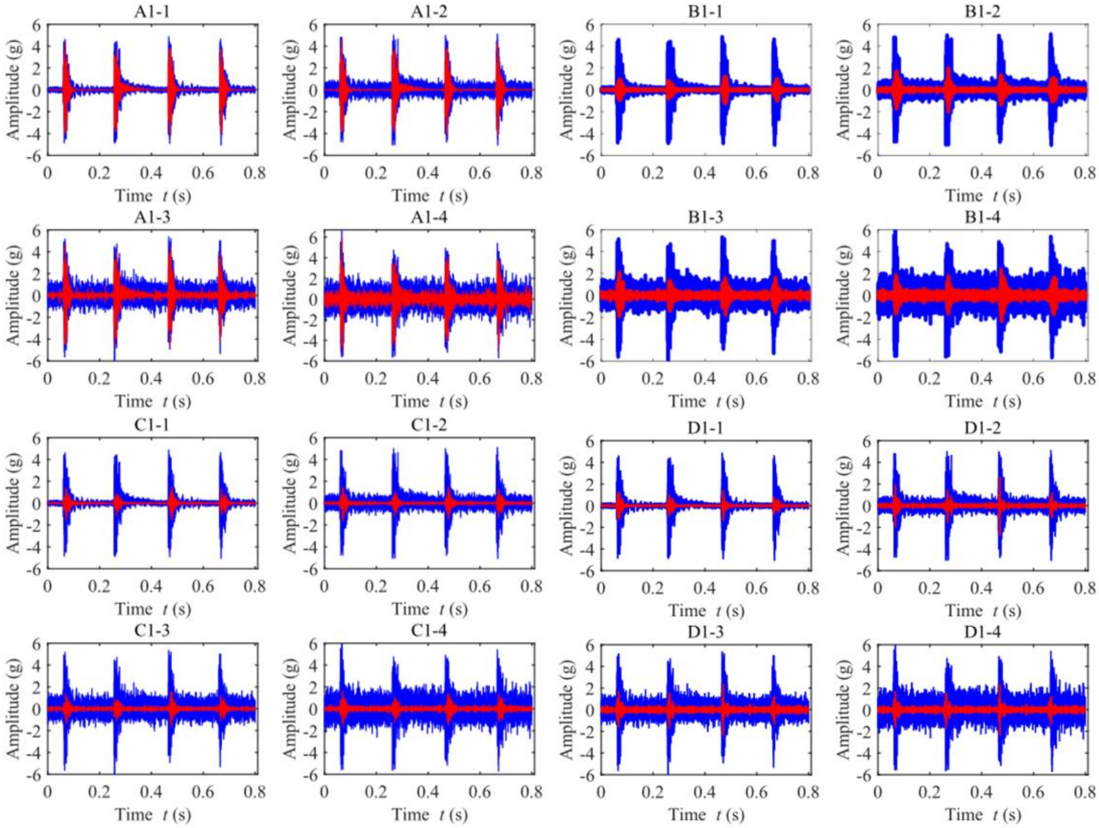

Fig. 9. Comparison of the effects of using ASNRA: A1-1~A1-4, using EMD: B1-1~B1-4, using EEMD: C1-1~C1-4, using VMD: D1-1~D1-4

Table 3. Performance comparison between denoising algorithms

Method	Noise Amplitude	Root Mean Square Error	Signal-to-Noise Ratio Before Denoising	Signal-to-Noise Ratio After Denoising	Signal-to-Noise Ratio Improvement Ratio
EMD	0.1	0.5770	-4.2971	-10.4280	-142.6%
	0.3	0.5429	-4.1330	-8.5532	-106.9%
	0.5	0.6001	-6.0499	-8.9579	-48.1%
	0.7	0.6143	-6.0155	-9.2738	-54.2%
EEMD	0.1	0.5478	-4.2971	-9.0291	-110.1%
	0.3	0.5313	-4.1330	-9.4894	-129.6%
	0.5	0.5682	-6.0499	-10.5859	-75.0%
	0.7	0.5647	-6.0155	-11.5203	-91.5%
VMD	0.1	0.5745	-4.2971	-13.1273	-205.5%
	0.3	0.5786	-4.1330	-10.7661	-160.5%
	0.5	0.5972	-6.0499	-11.1673	-84.6%
	0.7	0.5972	-6.0155	-13.5896	-125.9%
ASNRA	0.1	0.5456	-4.2971	1.0870	125.3%
	0.3	0.5659	-4.1330	-0.2846	93.1%

0.5	0.8076	-6.0499	-0.9614	84.1%
0.7	0.8724	-6.0155	-0.0416	99.3%

3.3.2 The evaluation index selection and internal setting for impact localization

Table 4 shows the detailed parameter configuration of RDSVR to predict the impact position in three cases: under the consideration of large searching space (C1), small searching space (C2) and the situation where result comparison is conducted between the proposed architecture and Bayesian optimization-based DSVR(C3). In the parameter selection process of the RDSVR, RMSE is chosen as the fitness function because it measures the difference between the predicted values of the RDSVR and the actual observed values. Compared to Mean Square Error (MSE) and R2, RMSE is highly sensitive to outliers due to the error of each data point. This means that one or more extreme outliers can significantly increase the value of RMSE, making it a measure of the RDSVR's stability. The formula is as follows:

$$Fitness = RMSE \tag{10}$$

$$RMSE = \sqrt{\frac{\sum_{i=1}^{M}(X_{pre,i} - X_{real,i})^2}{M}} \tag{11}$$

where $Fitness$ is the fitness function, M is the number of observations, $X_{pre,i}$ means the predicted data, and $X_{real,i}$ denotes the real data.

Table 4. Internal parameter setting of three types of cases

Case	Fitness	Population Size	Iteration Number	Update Dimensions	C	γ
C1	$RMSE$	100	50	2	1-10000	0.001-10
C2	$RMSE$	100	50	2	1-1000	0.01-2
C3	$RMSE$	100	100	2	1-1000	0.001-2

3.3.3 Result comparison between the proposed architecture and Metaheuristic Algorithms-based DSVR methods

This section mainly analyzes the results of IL in C1 and C2, to verify the global searching performance of the proposed IL architecture.

Since the four algorithms of Grey Wolf Optimizer (GWO)[40], Harris Hawks Optimization (HHO)[41], Slime Mould Algorithm (SMA)[27], and Hunger Games Search (HGS)[42] have the powerful global optimization ability and thus, they are selected to optimize the internal parameters of DSVR with the comparison of the performance of IL architecture in predicting the impact coordinate values. In this paper, GWO-optimized Dual-layer Support Vector Regression (GDSVR), HHO-optimized Dual-layer Support Vector Regression (HODSVR), SMA-optimized Dual-layer Support Vector Regression (SDSVR), and HSG-optimized Dual-layer Support Vector Regression (HSDSVR) are constructed to predict position of low-speed impact, dynamically optimizing the commonly used parameters γ and C as a basis for comparison. In these methods, parameters are unchanged in C1 and C2. Table 5 shows the kernel parameter γ and penalty parameter C obtained by the global optimization for the minimum fitness value in C1. It is noted that IL architecture yields the optimal RMSE of 4.7840. Results show that proposed architecture has good stability in positioning as fewer abnormal points with smaller errors are observed.

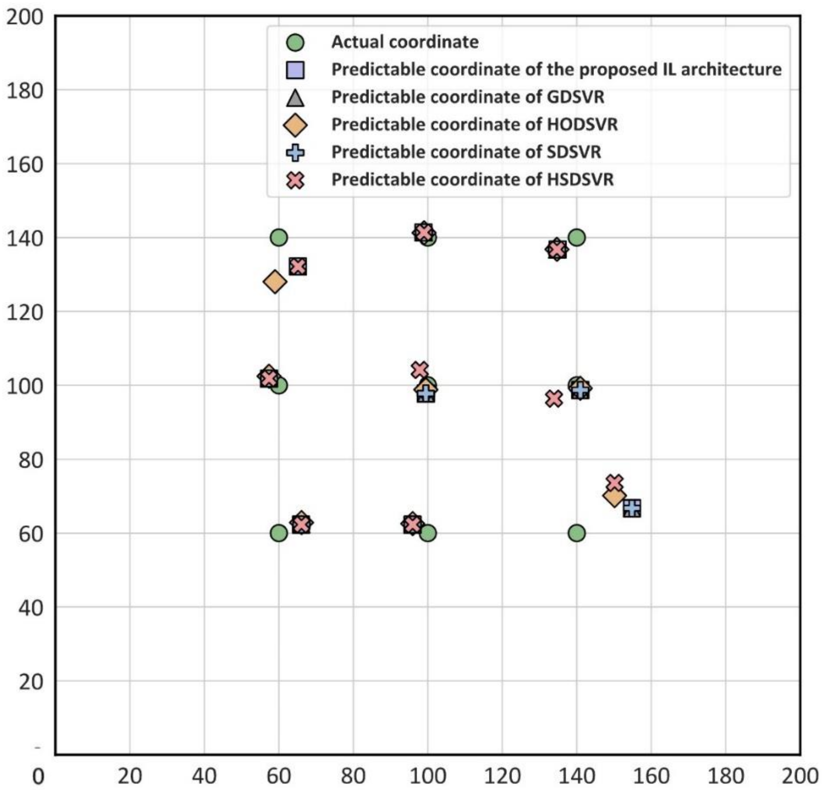

Fig. 10. Prediction results by five methods in C1

Table 5. The prediction results of IL at Points P1-P9 (in Fig. 5) by four methods in C1

IL architecture	GDSVR	HODSVR	SDSVR	HSDSVR	Actual coordinate

	x	y	x	y	x	y	x	y	x	y	x	y
P1	64.721	137.550	67.518	137.677	66.740	130.737	67.541	137.682	67.553	132.174	60	140
P2	97.980	138.812	107.784	138.983	103.258	137.633	107.815	138.964	107.838	141.357	100	140
P3	136.438	137.524	137.375	133.674	138.731	126.021	137.366	133.655	137.345	128.169	140	140
P4	57.496	100.601	57.705	103.743	54.493	102.578	56.326	106.017	53.937	102.597	60	100
P5	97.947	103.364	101.243	92.770	94.086	98.754	94.292	94.498	101.219	92.930	100	100
P6	140.738	98.953	137.780	98.886	138.4716	99.368	139.650	97.285	139.657	96.410	140	100
P7	65.015	62.852	61.318	66.989	61.625	69.587	61.329	66.997	61.337	68.976	60	60
P8	95.686	68.095	93.218	68.964	92.453	72.508	93.221	68.965	93.225	69.947	100	60
P9	155.280	63.554	155.977	64.210	157.325	66.156	155.955	64.168	155.937	66.730	140	60
C	1069.240	9166.749	10000.0	10000.0	5949.650	380.674	10000.0	10000.0	10000.0	903.124		
γ	0.046783	0.017191	0.016216	0.016328	0.020321	0.049629	0.016197	0.016344	0.016182	0.035706		
RMSE	4.7840		6.1590		7.6903		6.3508		7.3136			

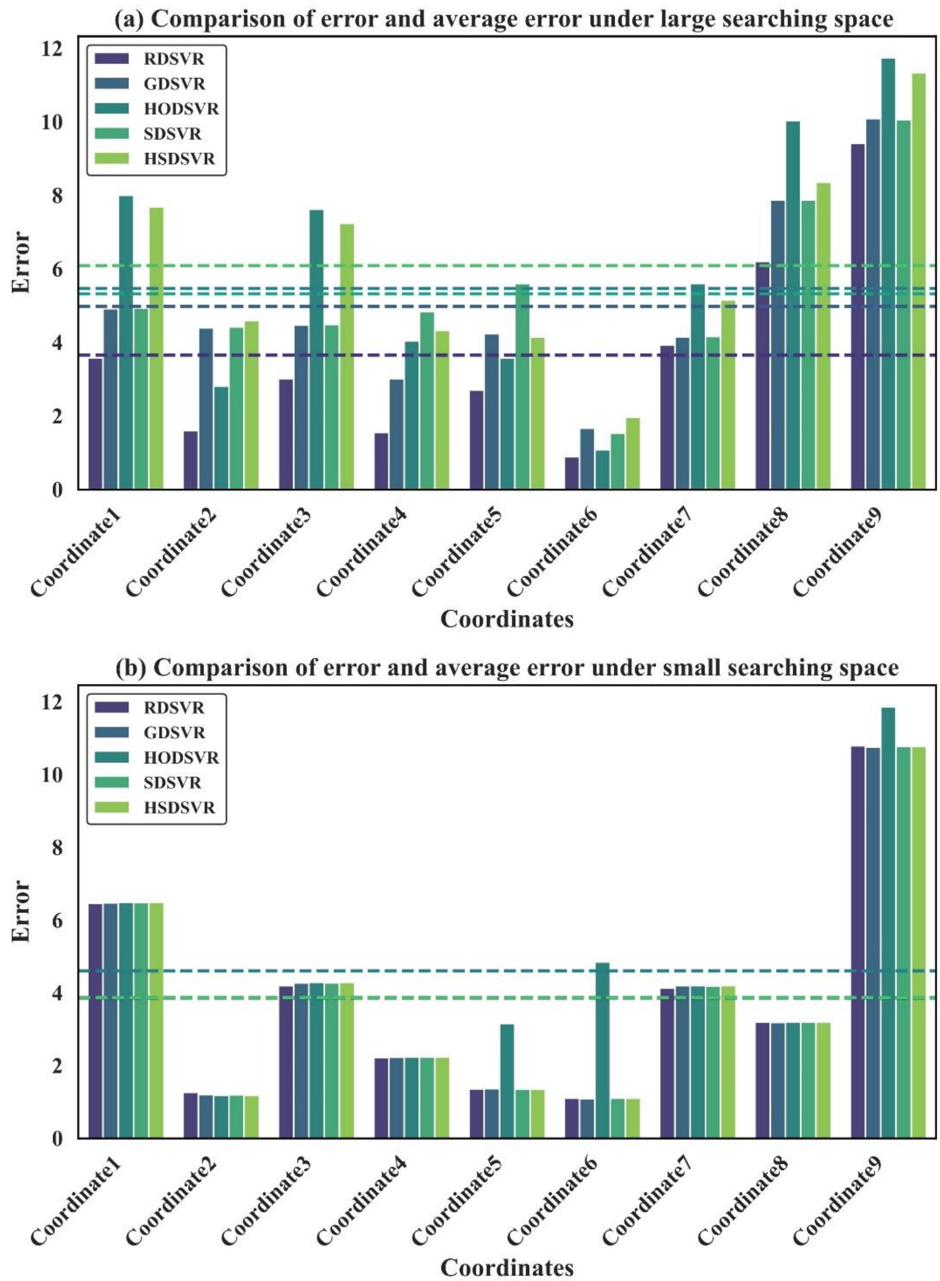

Fig. 11. Error Comparison by five aforementioned methods

It is observed in Fig.10 that as the smallest error is introduced by the proposed architecture, the best predictions at those 9 points are achieved. In Fig. 11, the five bar charts represent the single-point error under both C1 and C2, with the dashed lines showing the average error of the five methods. The average error by IL architecture is maintained at about 3.6 mm shown in Fig. 11(a), where the best overall prediction accuracy can be observed. The fewer errors from the predictions on 9 single points demonstrate that IL architecture is superior to other methods. With the additional consideration of the lowest RMSE, it is verified that in the proposed architecture, the fluctuates of prediction errors are least and the error is controlled within a certain range, while the error fluctuation of the predictions by other methods is larger and the accuracy is lower.

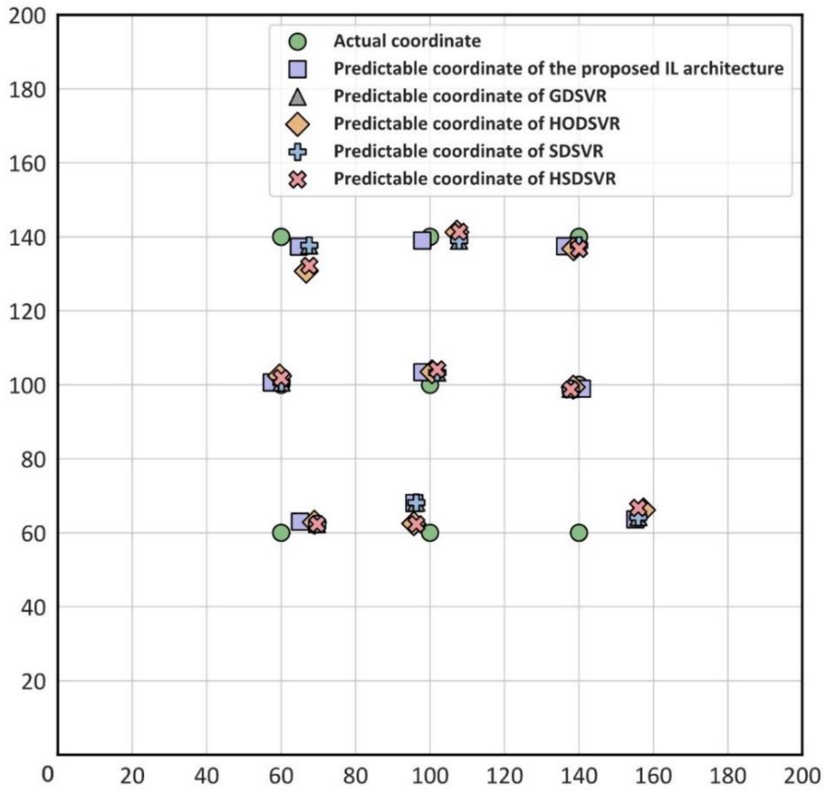

Fig. 12. The prediction points by five methods in C2

Table 6. The prediction results of IL at Points P1-P9 (in Fig. 5) by four methods in C2

Method Comparison	**RDSVR**		**GDSVR**		**HODSVR**		**SDSVR**		**HSDSVR**		**Actual coordinate**	
	x	y	x	y	x	y	x	y	x	y	x	y
P1	65.110	132.184	65.140	132.187	58.972	128.048	65.144	132.171	65.151	132.168	60	140
P2	98.834	141.367	98.945	141.359	98.990	141.274	98.960	141.357	98.988	141.356	100	140
P3	134.849	136.751	134.719	136.736	134.666	136.808	134.701	136.750	134.670	136.750	140	140
P4	57.377	101.826	57.368	101.836	57.365	102.459	57.367	101.839	57.365	101.840	60	100
P5	99.479	97.800	99.477	97.787	97.837	104.158	99.477	97.811	99.476	97.814	100	100
P6	140.937	98.719	140.944	98.757	133.899	96.406	140.945	98.731	140.947	98.730	140	100
P7	65.956	62.314	66.046	62.350	66.082	62.870	66.058	62.323	66.079	62.322	60	60
P8	95.917	62.305	95.925	62.302	95.928	62.570	95.926	62.314	95.927	62.315	100	60
P9	154.832	66.755	154.816	66.706	150.151	73.583	154.814	66.736	154.810	66.738	140	60
C	1000.0	912.957	1000.0	903.014	1000.0	396.254	999.998	903.414	1000.0	902.871		
γ	0.046766	0.035546	0.046622	0.035742	0.046564	0.048554	0.046603	0.035695	0.046567	0.035699		
RMSE	5.0160		5.0219		5.5936		5.0265		5.0291			

Fig. 12 shows that the proposed IL architecture predicts the impact coordinates of the reference point (100, 140) more accurately than other methods. According to the data in Fig. 11(b) and Table 6, the differences among the five methods in C2 are negligible, highlighting the stability of IL architecture. By performing the optimization of the parameter C, the proposed architecture tends to focus on the high-quality solutions globally while other methods determine the upper limit of the parameter C in C1. Consequently, it exhibits superior convergence performance, ensuring the reliability and stability in solving the cases of C1 and C2.

3.3.4 Result comparison between the proposed architecture and Bayesian-optimized DSVR method

Bayesian optimization exhibits excellent scalability in the process of hyperparameter optimization and also enables fast iterations and minimal counts, reducing time costs and providing robust global solutions to non-convex problem-solving[43]. In this section, a Bayesian-optimized Dual-layer support vector regression (BDSVR) is conducted for performance comparison with RDSVR to demonstrate the prediction accuracy and efficiency of RDSVR. The parameters C and γ in the SVR method are ranged from 1 to 10000 and 0.001 to 2, respectively. Fig.13 shows the IL by the proposed architecture have the similar degree of accuracy as the results by BDSVR. It should be noted that the proposed IL architecture ensures the exactly prediction at the point (100,60). In Table 7, it is evidenced that the proposed architecture achieves a better result with the RMSE value of 2.363 and outperforms BDSVR ($\text{RMSE} = 2.577$) by 9%, indicating that RDSVR has the superior ability to explore the global optimal solution and avoid falling into the local optimum. Fig. 14 describes the evolutionary history of the fitness values used to evaluate the optimal searching results using these two methods. The RDSVR fitness value curve of 50 iterations in Fig. 14 (a) and (c) shows a decreasing trend; however, the BDSVR fitness value curve considering 2000 iterations in Fig. 14 (b) and (d) will show a trend of oscillation. The above two phenomena show that the principle of proposed architecture is to continuously explore better results. BDSVR is to find various results in a certain interval. The difference in their principles also leads to better efficiency and accuracy of RDSVR in solving. In terms of the computational time, the IL architecture achieves the solution in 1,332.786 s, while BDSVR obtains the similar result by the increased time of 41% (1,880.331s). It is concluded that the proposed architecture significantly reduces computational time and enable both the robust convergence capability and improved accuracy, demonstrating the high effectiveness in solving large searching space problems. Furthermore, as the increase of dimensionality in the optimization process, the superiority of the proposed architecture over BDSVR for IL of composite structures becomes more pronounced.

Table 7. Result comparison between the proposed architecture and Bayesian-optimized DSVR

Multi working condition	**IL architecture**		**BDSVR**		**Actual coordinate**	
Impacts	x	y	x	y	x	y
P1	61.65	137.32	61.21	136.17	60	140
P2	99.12	138.79	99.99	140.01	100	140
P3	136.42	135.84	138.66	135.20	140	140
P4	62.09	100.15	61.19	100.50	60	100
P5	104.73	98.84	96.41	99.17	100	100
P6	144.08	101.67	135.45	100.24	140	100
P7	60.67	58.49	60.97	57.83	60	60
P8	99.34	60.36	105.62	59.31	100	60
P9	139.86	57.13	142.72	60.09	140	60
C	4761.502	8644.420	3053.830	9604.011		
γ	0.0175	0.0111	0.0260	0.0081		
Time	597.658	735.128	926.199	954.132		
Total Time	1,332.786		1,880.331			
RMSE	2.363		2.577			

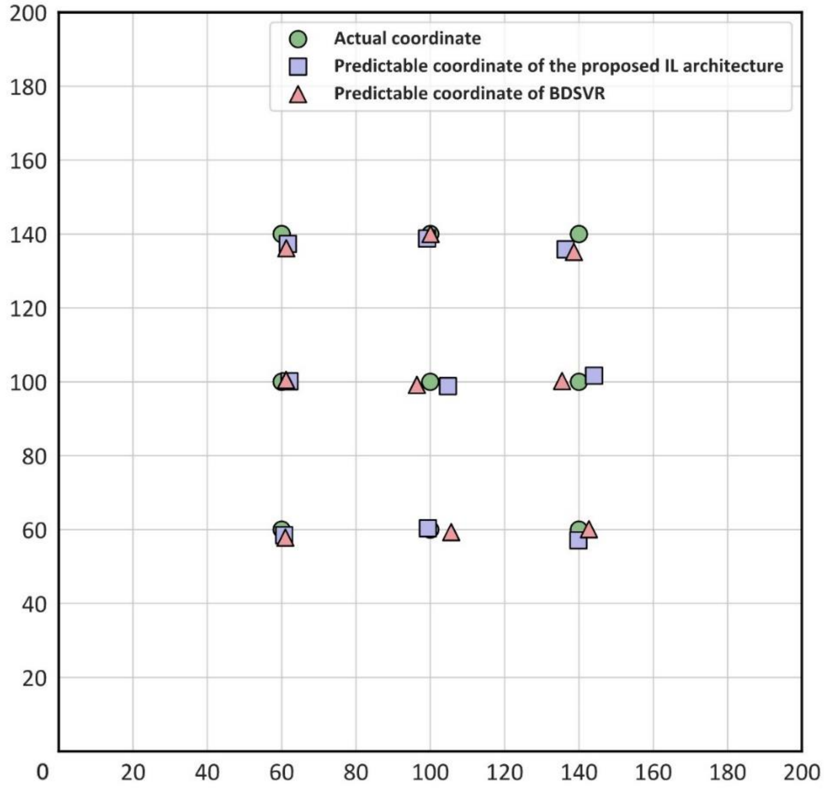

Fig. 13. Predictions of results by the proposed architecture and BDSVR

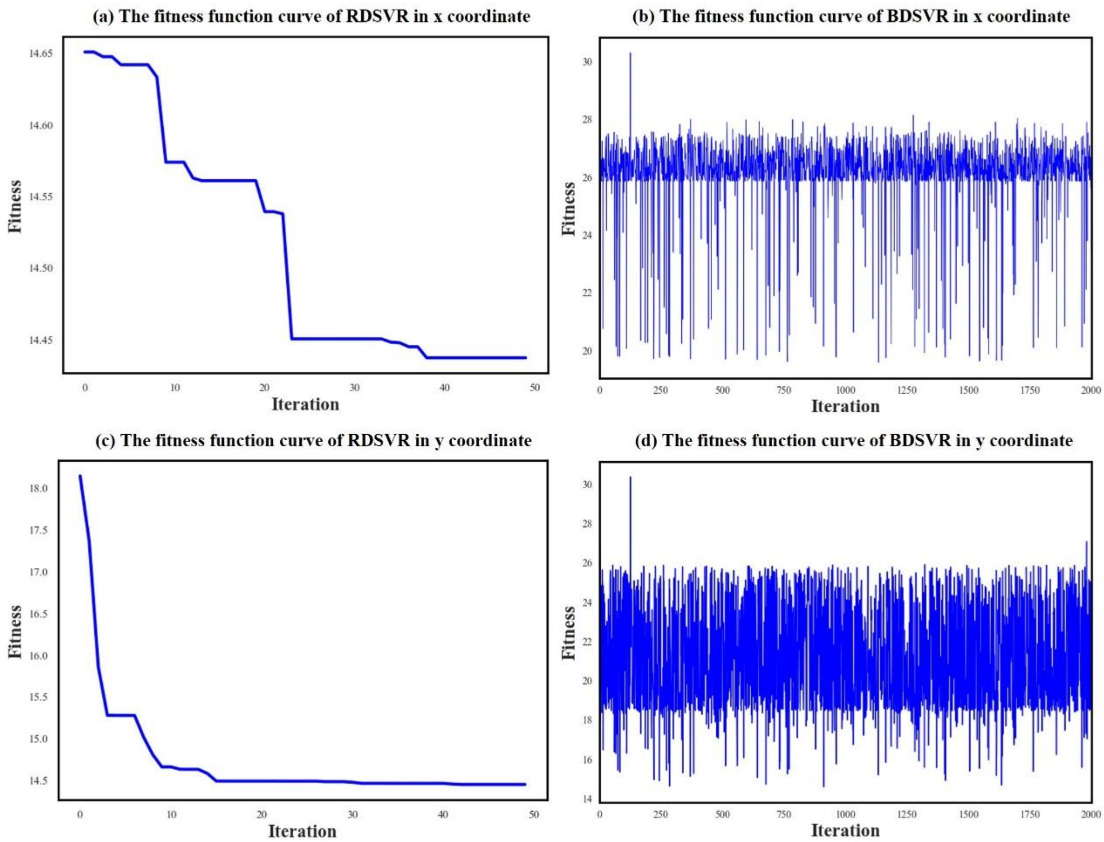

Fig. 14. Comparison of RDSVR and BDSVR fitness function

4. Conclusion

In this paper, a machine-learning architecture is proposed to realize the impact localization of composite laminates. The developed IL architecture has the ability to accurately and effectively predict the low-speed impact positions of composite laminates in the white noise environment with standard deviations of 0.1,0.3,0.5 and 0.7, respectively. As compared with other noise reduction algorithms, the signal-to-noise ratio rate by Adaptive Sparse Noise Reduction Algorithm(ASNRA) is improved over 84%, demonstrating the ASNRA with the capability of effectively extracting the feature amplitude under real working conditions. Meanwhile, the proposed architecture has the lowest RMSE with a fast convergence as compared with four metaheuristic optimization-based DSVR and Bayesian-optimized DSVR methods under the consideration of large and small searching space, verifying its the remarkably high suitability and computational efficiency. Throughout the experimental tests, the proposed architecture enables to accurately realize the impact localization of composite laminates and also lays a solid foundation on the development of novel algorithms for novel structural health monitoring.

References

[1] S. Choudhary, M.K. Sain, V. Kumar, P. Saraswat, M.K. Jindal, Advantages and applications of sisal fiber reinforced hybrid polymer composites in automobiles: A literature review, Materials Today: Proceedings, (2023).

[2] J.E.R. Dhas, M.E. Sahayaraj, K.A.S. Lewise, P. Akhil, A. Sudhakar, Design and fabrication of automobile wheel rim using composite materials, Materials Today: Proceedings, (2023).

[3] C. Garnier, M.-L. Pastor, F. Eyma, B. Lorrain, The detection of aeronautical defects in situ on composite structures using Non Destructive Testing, Composite structures, 93 (2011) 1328-1336.

[4] K.B. Katnam, L. Da Silva, T. Young, Bonded repair of composite aircraft structures: A review of scientific challenges and opportunities, Progress in Aerospace Sciences, 61 (2013) 26-42.

[5] H. Zhang, H. Yu, C. Sun, Y. Tong, J. Deng, L. Wu, L. Sun, S. Guo, H. Liu, Evaluation of new hydrophobic association inorganic composite material as coagulant for oilfield wastewater treatment, Separation and Purification Technology, 275 (2021) 119126.

[6] M. Chairi, J. El Bahaoui, T. Alderucci, F. Favaloro, C. Borsellino, G. Di Bella, Preliminary study of lightweight fibre-ceramic composite structures for the ballistic protection on military vessels, Procedia CIRP, 118 (2023) 810-815.

[7] M. Strąg, W. Świderski, Non-destructive inspection of military-designated composite materials with the use of Terahertz imaging, Composite Structures, 306 (2023) 116588.

[8] H. Yang, L. Yang, Z. Yang, Y. Shan, H. Gu, J. Ma, X. Zeng, T. Tian, S. Ma, Z. Wu, Ultrasonic detection methods for mechanical characterization and damage diagnosis of advanced composite materials: A review, Composite Structures, (2023) 117554.

[9] J. Rafiee, F. Arvani, A. Harifi, M. Sadeghi, Intelligent condition monitoring of a gearbox using artificial neural network, Mechanical systems and signal processing, 21 (2007) 1746-1754.

[10] Q. Liu, F. Wang, W. Xiao, J. Cui, Binary dynamic stochastic search algorithm with support vector regression for feature selection in low-velocity impact localization problem, Engineering Applications of Artificial Intelligence, 124 (2023) 106554.

[11] D. Meng, H. Wang, S. Yang, Z. Lv, Z. Hu, Z. Wang, Fault analysis of wind power rolling bearing based on EMD feature extraction, CMES-Computer Modeling in Engineering & Sciences, 130 (2022) 543-558.

[12] Y. Jia, G. Li, X. Dong, K. He, A novel denoising method for vibration signal of hob spindle based on EEMD and grey theory, Measurement, 169 (2021) 108490.

[13] G. Mousmoulis, C. Yiakopoulos, G. Aggidis, I. Antoniadis, I. Anagnostopoulos, Application of Spectral Kurtosis on vibration signals for the detection of cavitation in centrifugal pumps, Applied Acoustics, 182 (2021) 108289.

[14] D. Zhang, D. Zhang, Wavelet transform, Fundamentals of image data mining: Analysis, Features, Classification and Retrieval, (2019) 35-44.

[15] M. Rhif, A. Ben Abbes, I.R. Farah, B. Martínez, Y. Sang, Wavelet transform application for/in non-stationary time-series analysis: A review, Applied Sciences, 9 (2019) 1345.

[16] C. Yin, Y. Wang, G. Ma, Y. Wang, Y. Sun, Y. He, Weak fault feature extraction of rolling bearings based on improved ensemble noise-reconstructed EMD and adaptive threshold denoising, Mechanical Systems and Signal Processing, 171 (2022) 108834.

[17] H. Li, T. Liu, X. Wu, S. Li, Research on test bench bearing fault diagnosis of improved EEMD based on improved adaptive resonance technology, Measurement, 185 (2021) 109986.

[18] S. Hashim, P. Shakya, A spectral kurtosis based blind deconvolution approach for spur gear fault diagnosis, ISA transactions, 142 (2023) 492-500.

[19] Q. Liu, F. Wang, J. Li, W. Xiao, A hybrid support vector regression with multi-domain features for low-velocity impact localization on composite plate structure, Mechanical Systems and Signal Processing, 154 (2021) 107547.

[20] J. Lu, B. Wang, D. Liang, Wavelet packet energy characterization of low velocity impacts and load localization by optical fiber Bragg grating sensor technique, Applied optics, 52 (2013) 2346-2352.

[21] A. Datta, M. Augustin, N. Gupta, S. Viswamurthy, K.M. Gaddikeri, R. Sundaram, Impact localization and severity estimation on composite structure using fiber bragg grating sensors by least square support vector regression, IEEE Sensors Journal, 19 (2019) 4463-4470.

[22] K. Mehmood, N.I. Chaudhary, Z.A. Khan, K.M. Cheema, M.A.Z. Raja, C.-M. Shu, Novel knacks of chaotic maps with Archimedes optimization paradigm for nonlinear ARX model identification with key term separation, Chaos, Solitons & Fractals, 175 (2023) 114028.

[23] D. Karaboga, An idea based on honey bee swarm for numerical optimization, Technical report-tr06, Erciyes university, engineering faculty, computer …, 2005.

[24] X.-S. Yang, A new metaheuristic bat-inspired algorithm, Nature inspired cooperative strategies for optimization (NICSO 2010), Springer, 2010, pp. 65-74.

[25] S. Mirjalili, A. Lewis, The whale optimization algorithm, Advances in engineering software, 95 (2016) 51-67.

[26] S. Saremi, S. Mirjalili, A. Lewis, Grasshopper optimisation algorithm: theory and application, Advances in engineering software, 105 (2017) 30-47.

[27] S. Li, H. Chen, M. Wang, A.A. Heidari, S. Mirjalili, Slime mould algorithm: A new method for stochastic optimization, Future Generation Computer Systems, 111 (2020) 300-323.

[28] K. Chen, Q. Liao, K. Liu, Y. Yang, G. Gao, G. Wu, Capacity degradation prediction of lithium-ion battery based on artificial bee colony and multi-kernel support vector regression, Journal of Energy Storage, 72 (2023) 108160.

[29] A.-L. Balogun, F. Rezaie, Q.B. Pham, L. Gigović, S. Drobnjak, Y.A. Aina, M. Panahi, S.T. Yekeen, S. Lee, Spatial prediction of landslide susceptibility in western Serbia using hybrid support vector regression (SVR) with GWO, BAT and COA algorithms, Geoscience Frontiers, 12 (2021) 101104.

[30] H. Xian, J. Che, Unified whale optimization algorithm based multi-kernel SVR ensemble learning for wind speed forecasting, Applied Soft Computing, 130 (2022) 109690.

[31] Z.Y. Algamal, M.K. Qasim, M.H. Lee, H.T.M. Ali, Improving grasshopper optimization algorithm for hyperparameters estimation and feature selection in support vector regression, Chemometrics and Intelligent Laboratory Systems, 208 (2021) 104196.

[32] M. Awad, R. Khanna, M. Awad, R. Khanna, Support vector regression, Efficient learning machines: Theories, concepts, and applications for engineers and system designers, (2015) 67-80.

[33] J. Hu, B. Guo, N. Liao, Z. Yi, S. Zhang, W. He, Magnetic anomaly feature extraction using the tunable Q-factor wavelet transform based on non-convex overlapping group shrinkage, Journal of Physics: Conference Series, IOP Publishing, 2020, pp. 012040.

[34] W. Teng, Y. Liu, Y. Huang, L. Song, Y. Liu, Z. Ma, Fault detection of planetary subassemblies in a wind turbine gearbox using TQWT based sparse representation, Journal of Sound and Vibration, 490 (2021) 115707.

[35] M. Nikolova, Energy minimization methods, Handbook of mathematical methods in imaging, (2011) 138-186.

[36] S. Wang, I. Selesnick, G. Cai, Y. Feng, X. Sui, X. Chen, Nonconvex sparse regularization and convex optimization for bearing fault diagnosis, IEEE Transactions on Industrial Electronics, 65 (2018) 7332-7342.

[37] C. Mateo, J.A. Talavera, Short-time Fourier transform with the window size fixed in the frequency domain (STFT-FD): Implementation, SoftwareX, 8 (2018) 5-8.

[38] Y.-G. Wang, J. Wu, Z.-H. Hu, G.J. McLachlan, A new algorithm for support vector regression with automatic selection of hyperparameters, Pattern Recognition, 133 (2023) 108989.

[39] H. Su, D. Zhao, A.A. Heidari, L. Liu, X. Zhang, M. Mafarja, H. Chen, RIME: A physics-based optimization, Neurocomputing, 532 (2023) 183-214.

[40] S. Mirjalili, S.M. Mirjalili, A. Lewis, Grey wolf optimizer, Advances in engineering software, 69 (2014) 46-61.

[41] A.A. Heidari, S. Mirjalili, H. Faris, I. Aljarah, M. Mafarja, H. Chen, Harris hawks optimization: Algorithm and applications, Future generation computer systems, 97 (2019) 849-872.

[42] Y. Yang, H. Chen, A.A. Heidari, A.H. Gandomi, Hunger games search: Visions, conception, implementation, deep analysis, perspectives, and towards performance shifts, Expert Systems with Applications, 177 (2021) 114864.

[43] A. Klein, S. Falkner, S. Bartels, P. Hennig, F. Hutter, Fast bayesian optimization of machine learning hyperparameters on large datasets, Artificial intelligence and statistics, PMLR, 2017, pp. 528-536.